Tracking the spread of chaos in the swinging Atwood's machine

Nick Tufillaro
aqualytics.eco
P.O. Box 1028
Corvallis, OR 97333
nick@aqualytics.eco
orcid #: 0009-0006-2896-8832

May 13, 2026

Abstract

Chaos is investigated in the swinging Atwood's machine (SAM) as the mass ratio, μ, decreases away from the integrable motion at $\mu = 3$ down to mostly chaotic dynamics at $\mu = 2.7$. The spread of chaos is characterized by combining a stability index with a Poincaré surface of section (SOS). An effective computational solution requires detailed consideration of a few numeric overflow issues. Once these are resolved, the computational study shows that the spread of chaos, in this parameter regime, is associated with a hyperbolic periodic "loop" orbit. The problem illustrates how to incorporate some computational physics considerations, such as the regularization of a singularity, into a junior-level classical mechanics course.

1 Introduction

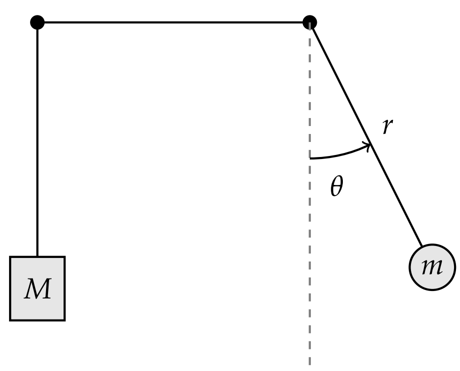

Figure 1: The swinging Atwood's machine.

The swinging Atwood's machine (SAM) is a tractable problem both theoretically [1] and experimentally [2, 3] for undergraduates studying classical mechanics. Recall that for SAM, one of the masses (m) is allowed to swing in the plane (Fig. 1). Assuming the masses are connected by frictionless, massless pulleys, the Hamiltonian for SAM is:

$$H = \frac{1}{2}\left(\frac{p_r^2}{\mu+1} + \frac{p_\theta^2}{r^2}\right) + gr(\mu - \cos\theta) \tag{1}$$

where p_r and p_θ are the conjugate momenta, g is gravitational acceleration, and $\mu = M/m$ is the mass ratio. We want to focus on how the dynamics depend on the parameter μ – so, without loss of generality, we set $m = 1$ in the Hamiltonian, which effectively just rescales the energy. Since the potential function is homogeneous, orbits at different energy levels are similar [4].

SAM is integrable for the mass ratio $\mu = 3$, and provably chaotic for all other mass ratios [5,6]. Integrable Hamiltonian systems are stratified by KAM tori [7], which allows for the solution of all periodic and quasiperiodic orbits in terms of the rotation number [8]. As we perturb away from this integrable motion, however, tori dissolve (based on stability conditions which are a function of the rotation number [9–11]), and stable regions of phase space (periodic or quasi-periodic orbits) are replaced by unstable regions (chaotic orbits).

In this paper, we examine how chaos spreads as the mass ratio decreases away from the integrable (stable) motion, specifically as mass decreases from 3 to 2.7. Numerical experiments reveal that the geometric feature governing the spread of chaos in this parameter regime is an unstable periodic orbit associated with a collision between the swinging mass and the pulley. In the lingo of dynamical systems, chaos spreads as part of the bifurcation process leading to the merger of an unstable homoclinic orbit and its elliptical partner – a saddle-center bifurcation of periodic orbits – and the regions of stable and chaotic orbits are roughly delineated by the stable and unstable manifolds of this homoclinic orbit [12]. From a physical point of view, this mechanism of chaos is easy to visualize – orbits that start very close are suddenly far apart after they fly off to the left, or to the right, during a near collision with the pulley. This is analogous to the origin of chaos in a forced pendulum, where orbits approaching the unstable equilibrium (the inverted pendulum) fall chaotically to the left or right, depending on the system's state.

To investigate chaos in SAM, we proceed in the normal way [13, 14]. First, we visualize the global dynamics as a function of μ using a Poincaré surface of section (SOS) [15]. On the surface of section we identify stable regions (periodic or quasiperiodic orbits) and unstable regions (chaotic orbits), both qualitatively and quantitatively by coloring the orbit based on their stability, estimated using the Smaller Alignment Index (SALI) [16]. We identify geometrical structures in the phase space, namely the low-order periodic orbits and their stable and unstable manifolds, that shephard the flow as μ is varied from 3 (integrable) to 2.7 (mostly chaotic), and track the overall spread of chaos using the SALI. The theoretical and computational aspects are well covered in pedagogical books and papers [17–20], as well as commonly available numerical toolkits [21–24], so we will not delve much into the methods here, except for two aspects of the computational solution.

Namely, in Section 2, we discuss 'regularization' – or how to deal with the 'division by zero' in the dynamical equations, and in Section 3, we discuss 'variational integration' – or how to handle overflow in the Jacobian Matrix through continuous normalization. After resolving these computational issues, we move on to Section 4, which presents the results on tracking the initial breakdown of the integrable motion. Although details vary from problem to problem, properly identifying and solving issues of overflow or underflow are ubiquitous in computational physics, and investigating the spread of chaos in SAM provides an introduction to some of the numeric challenges.

Problem 1: *Derive the equations of motion ($\dot{r}, \dot{\theta}, \dot{p}_r, \dot{p}_\theta$) for SAM from the Hamiltonian (Eq. 1). Use the energy contant, E, to develop a formula for $p_r = K(E, g, \mu, r, \theta, p_\theta)$ Using your function, K, write a* *script to integrate and plot (r, θ), for a few orbits for SAM assuming $g = 9.81$, $E = 2g$, $\theta_0 = 0$, and period, T. Some initial conditions to explore are (μ, r_0, p_{r0}, T): (a) $(3, 0.50, 6.26, 2.49)$, (b) $(2.95, 0.51, 6.08, 2.54)$, (c) $(2.99, 0.10, 0.73, 2.56)$, (d) $(2.95, 0.19, 1.52, 2.58)$, (e) $(2.95, 0.51, 5.84, 100)$, and (f) $(2.95, 0.125, 2.61, 100)$.*

2 Fixing the collision singularity

To construct a SOS, we need to numerically solve trajectories for a long time. However, a severe numerical issue arises because as the swinging mass approaches the pulley ($r \to 0$), the angular velocity $\dot{\theta} = p_\theta / r^2$ rapidly approaches infinity. This $1/r^2$ singularity instantly crashes standard numerical ODE solvers due to infinite derivatives and truncation errors.

To fix this, we use the mathematical technique known as 'regularization' – originally developed for astronomical simulations [25] – which consists of introducing a new fictitious time variable, τ, which is related to physical time t by the transformation:

$$dt = r^2 d\tau \tag{2}$$

Using this, we construct an extended phase space Γ which includes physical time, t, as a state variable:

$$\Gamma = r^2(H - E) = \frac{r^2 p_r^2}{2(1+\mu)} + \frac{1}{2} p_\theta^2 + g r^3 (\mu - \cos\theta) - E r^2 = 0 \tag{3}$$

With the new time τ, we obtain the regularized equations of motion (denoted by primes $d/d\tau$):

$$r' = \frac{\partial \Gamma}{\partial p_r} = \frac{r^2 p_r}{1+\mu} \tag{4}$$

$$\theta' = \frac{\partial \Gamma}{\partial p_\theta} = p_\theta \tag{5}$$

$$p_r' = -\frac{\partial \Gamma}{\partial r} = -\frac{r p_r^2}{1+\mu} - 3 g r^2 (\mu - \cos\theta) + 2 E r \tag{6}$$

$$p_\theta' = -\frac{\partial \Gamma}{\partial \theta} = -g r^3 \sin\theta \tag{7}$$

$$t' = \frac{\partial \Gamma}{\partial (-E)} = r^2 \tag{8}$$

Even if the mass passes exactly through the pulley ($r = 0$), the right-hand sides remain well-behaved, transitioning without blowing up to infinity.

The new variable effectively slows down time near the collision. This makes fixed-step-size simulations very inefficient. Therefore, an adaptive step-size method is required to solve the equations using regularization. In this study, we used the Dormand-Prince (RK45) method [26]. The adaptive solver shrinks or grows the step size in fictitious time τ by comparing the difference between the 4th and 5th-order to tight relative and absolute tolerances (10^{-8} and 10^{-10}, respectively).

Problem 2: *Transform the equations of motion using the regularization transform to arrive at Eqs. 4-8. Is the system described by Γ Hamiltonian (Eq. 3)? Is the regularization transform a 'canonical transformation' [1] .*

A Poincaré surface of section reduces the complexity of the 4D phase space $(r, \theta, p_r, p_\theta)$ down to a 2D plot. Because energy, E, is conserved, the accessible states are restricted to a 3D "energy shell" [27]. We take a 2D "slice" through this shell by recording the system state only when it crosses a specific geometric plane. In our analysis this is defined at $\theta = 0$ (the pendulum hanging straight down) while the mass crosses moving in the positive angular direction ($p_\theta > 0$). The resulting intersections are plotted in the remaining coordinates (r, p_r), which define a (nonglobal [15]) Poincaré surface of section.

Solving for a grid of initial conditions (r_0, p_{r0}) while varying μ (with fixed E) allows us to explore how the global dynamics depend on μ. Regions with continuous curves on the SOS indicate stable, quasi-periodic invariant tori, while scattered "dust" indicates unstable regions with chaotic orbits.

3 Distinguishing stable from unstable orbits

To evaluate the stability of an orbit, we look at the evolution of small perturbations using the "variational equations" constructed with the Jacobian matrix. Consider an n-dimensional continuous dynamical system defined by the system of ordinary differential equations:

$$\frac{d\mathbf{x}}{dt} = \mathbf{f}(\mathbf{x}(t)) \tag{9}$$

where $\mathbf{x} \in \mathbb{R}^n$ represents the state vector. Let $\mathbf{x}(t)$ be the reference trajectory, and $\mathbf{x}(t) + \mathbf{w}(t)$ be a perturbed trajectory. Linearizing the dynamics via a Taylor expansion yields the variational equations:

$$\frac{d\mathbf{w}}{dt} = J(\mathbf{x}(t))\,\mathbf{w}(t) \tag{10}$$

where $J(\mathbf{x}) = \frac{\partial \mathbf{f}}{\partial \mathbf{x}}$ is the $n \times n$ Jacobian matrix evaluated along the reference trajectory.

Problem 3: *The initial conditions (a)-(d) in Problem 1 are periodic orbits. Use these orbits as seed values to use in a 'root finding' algorithm with 'analytic continuation' to track the location of these orbits as μ varies from 3 down to 2.77, in steps of 0.01. Provide a list containing μ, the initial conditions, the period, the eigenvalues, and a classification of the orbit type (elliptic, hyperbolic). Use a toolbox like pynamicalsys [24] or develop your own code with the method outlined in Appendix A [28].*

In a chaotic regime, the distance between infinitesimally close trajectories diverges exponentially. Mathematically, the magnitude of the deviation vector grows as $||\mathbf{w}(t)|| \sim e^{\lambda_1 t}$, where $\lambda_1 > 0$ is the Maximum Lyapunov Exponent. When integrating these equations numerically using standard double-precision floating-point arithmetic (which caps at approximately 10^{308}), chaotic orbits will cause $||\mathbf{w}(t)||$ to overflow, resulting in a `NaN` (Not a Number) system failure within seconds.

However, as described below, to distinguish chaotic orbits from stable orbits, we only need to track the *direction* of the deviation vectors, not their magnitude. So we can restrict the solver to integrating unit vectors $\hat{\mathbf{w}} = \mathbf{w}/||\mathbf{w}||$. While discrete normalization at each integration step is an option, a numerically stable approach is continuous normalization built directly into the ODEs. Taking the time derivative of $\hat{\mathbf{w}}$:

$$\frac{d}{dt}\hat{\mathbf{w}} = \frac{d}{dt}\left(\frac{\mathbf{w}}{(\mathbf{w}^T\mathbf{w})^{1/2}}\right) \tag{11}$$

Applying the quotient rule and substituting $\dot{\mathbf{w}} = J\mathbf{w}$:

$$\frac{d\hat{\mathbf{w}}}{dt} = \frac{\dot{\mathbf{w}}}{||\mathbf{w}||} - \frac{\mathbf{w}}{||\mathbf{w}||^3}(\mathbf{w}^T\dot{\mathbf{w}}) = J\hat{\mathbf{w}} - \hat{\mathbf{w}}\left(\hat{\mathbf{w}}^T J\hat{\mathbf{w}}\right) \tag{12}$$

This equation acts as an intrinsic Gram-Schmidt orthogonal projection. The term $(\hat{\mathbf{w}}^T J\hat{\mathbf{w}})\hat{\mathbf{w}}$ subtracts any growth in the direction of $\hat{\mathbf{w}}$, mathematically guaranteeing that $\frac{d}{dt}||\hat{\mathbf{w}}||^2 = 0$. By appending this equation to the physical state equations, floating-point overflow is eliminated.

The Smaller Alignment Index (SALI) method takes advantage of the stretching nature of chaotic phase space to quickly distinguish between stable and unstable orbits [16]. Suppose we initialize two independent, orthonormal deviation vectors, $\hat{\mathbf{w}}_1(0)$ and $\hat{\mathbf{w}}_2(0)$. In a stable/quasiperiodic orbit, the motion is confined to an invariant torus. Without an exponentially dominant stretching direction, the two deviation vectors fluctuate and drift, but they remain linearly independent and do not permanently align. In an unstable/chaotic orbit, the phase space possesses at least one direction of exponential stretching. As the system evolves, the flow aggressively pulls both $\hat{\mathbf{w}}_1$ and $\hat{\mathbf{w}}_2$ to point along the direction of maximal expansion. Because the vectors are normalized, they will either become identical (parallel) or exact opposites (anti-parallel) (Fig. 2).

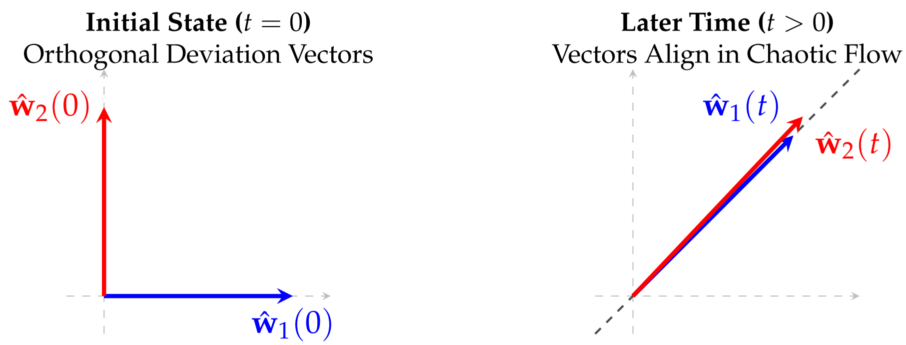

Figure 2: The Smaller Alignment Index (SALI) tracks alignment of perturbation vectors. Initially orthogonal vectors (left) are stretched by a chaotic flow (right), eventually aligning parallel to the axis of maximal expansion.

To quantify this geometric alignment, the Smaller Alignment Index is defined as the minimum between the sum and the difference of the two normalized deviation vectors:

$$\mathrm{SALI}(t) = \min\left(||\hat{\mathbf{w}}_1(t) + \hat{\mathbf{w}}_2(t)||,\ ||\hat{\mathbf{w}}_1(t) - \hat{\mathbf{w}}_2(t)||\right) \tag{13}$$

If the vectors align parallel ($\hat{\mathbf{w}}_1 \to \hat{\mathbf{w}}_2$), their difference approaches zero. If they align anti-parallel ($\hat{\mathbf{w}}_1 \to -\hat{\mathbf{w}}_2$), their sum approaches zero. In either case, the SALI plummets.

Problem 4: *Using the quasiperiodic initial condition from Problem 1(e), and the chaotic initial condition from Problem 1(f), create a figure like that shown in Fig. 3, illustraing how the SALI varies in time, and can be used to distinguish quasiperiodic orbits from chaotic orbits (see Appendix B).*

4 Tracking the spread of chaos

To track the spread of chaos in SAM, we estimate the percentage of unstable orbits to the total number of orbits by numerically sampling phase space using the surface of section.This is illustrated in Figure 4, which shows how phase space contains a greater percentage of chaotic orbits as we move away from the integrable motion at $\mu = 3$ to μ = 2.9, 2.8, and 2.7. The stability of each orbit in the SOS is evaluated and colored according to its estimated stability index. In the color map, a blue hue indicates stability and a red hue instability. A single threshold is applied to the stability index ($\log_{10}(\mathrm{SALI}) < -8$) to quantitatively evaluate the "spread" of chaos. The percentage is considered to be a simple estimate; a range of percentages is possible depending on the exact parameters chosen, however, the overall trends (increasing, decreasing) are assumed to be similar for reasonable choices of parameters.

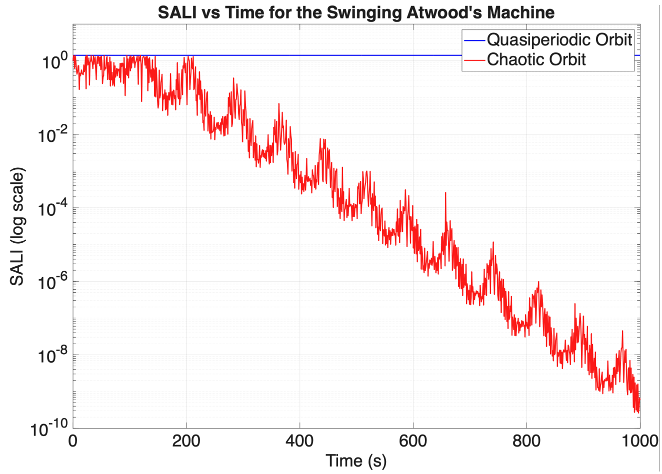

Figure 3: An example of how Smaller Alignment Index (SALI) as a function of time can distinguish between quasiperiodic (stable) and chaotic (unstable) orbits in the swinging Atwood's machine. Initial conditions from Problem 1(e, quasiperiodic), and Problem 1(f, chaotic), are used.

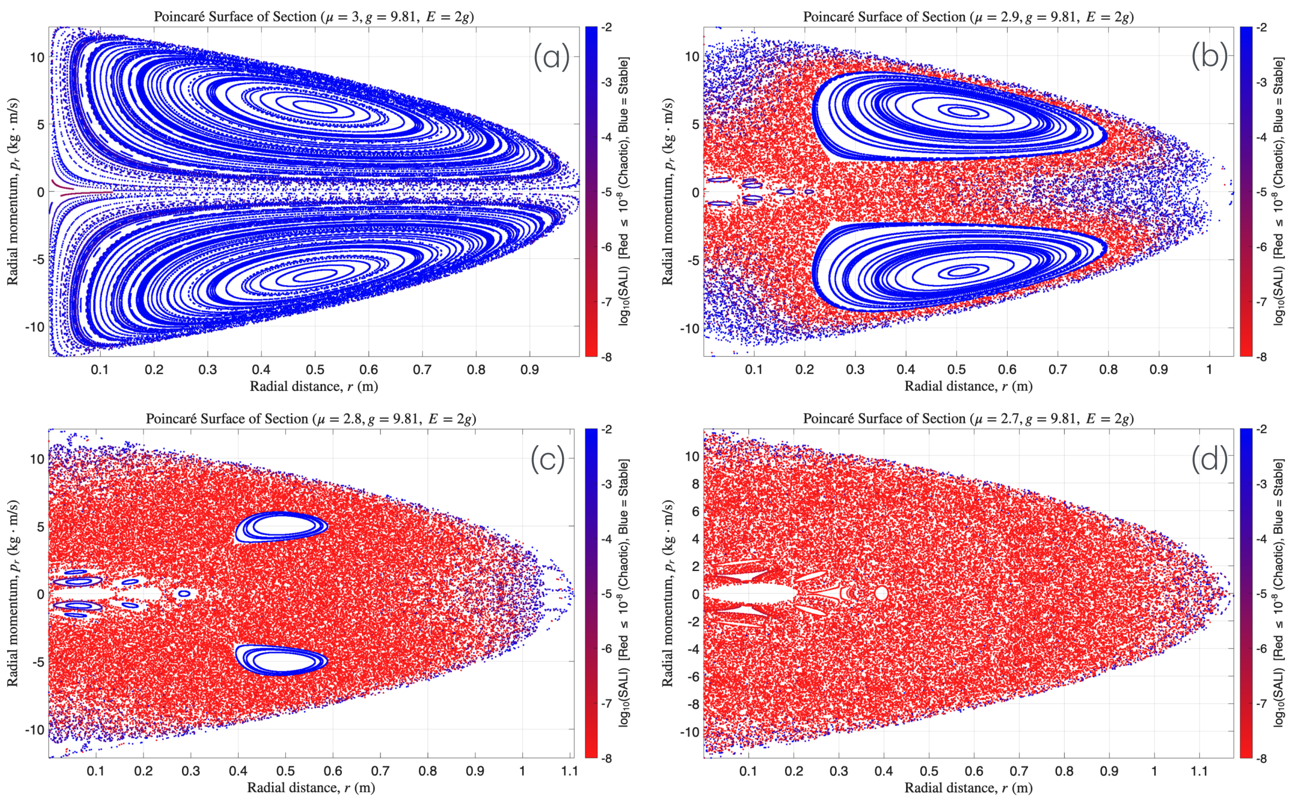

Figure 4: A sequence of surfaces of section for decreasing mass ratios (a) $\mu = 3$, integrable, stratified by tori (b) $\mu = 2.9$, nonintegrable, KAM tori and chaos (c) $\mu = 2.8$, increasingly chaotic as tori are destoryed (d) $\mu = 2.7$, mostly chaotic.

Figure 5 shows a plot of the spread of chaos as μ decreases from 3 down to 2.7. As indicated by the visual inspection, the percentage of phase space occupied by chaotic orbits decreases (more or less) monotonically from $\mu = 3$ to 2.7. Indeed, with a basic grounding in dynamical systems, it is easy to identify the geometrical mechanism causing the spread of the chaos – namely, a low-order hyperbolic periodic orbit that moves toward its partner elliptic periodic orbit, and in the process appears to destroy KAM tori as it approaches a saddle-center bifurcation, which the numerics indicate occurs at $\mu \approx 2.77$. This is an instance of what has been called "separatix chaos" [29, 30].

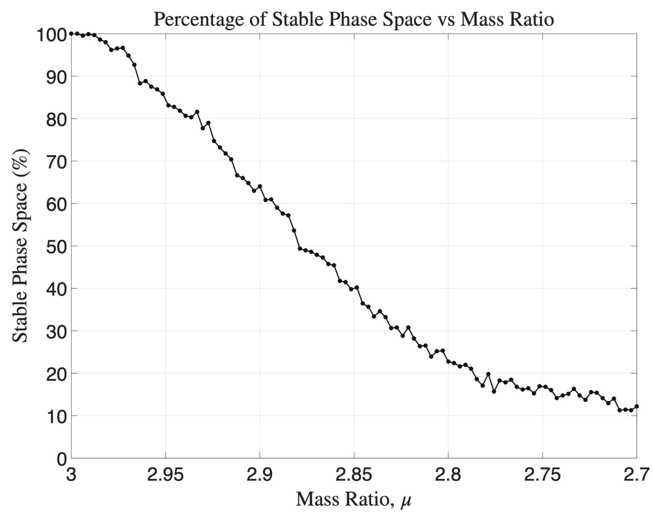

Figure 5: Estimated percentage of phase space with stable orbits as a function of the mass ratio, μ

In the study of dynamical systems, a "separatrix" is a boundary in phase space that divides distinct types of motion [13, 19]. Consider a pendulum [18, 31]. It has two primary modes of behavior: libration – small oscillations around the stable equilibrium (the bottom), and rotation – full circular revolutions (when given enough energy). The curve that separates these two behaviors is the separatrix. Physically, it represents the trajectory where the pendulum has exactly enough energy to reach the upright vertical position and stay there (an unstable equilibrium). In an ideal, integrable system (like the frictionless pendulum), the separatrix is a smooth, well-defined boundary. However, when a small perturbation is applied, the separatrix also points to a generic mechanism to generate chaos. The approach to the unstable position along the separatix (an unstable equilibrium point in the pendulum, or an unstable periodic orbit in SAM) can result in the system becoming extremely sensitive to even the smallest external influence near this boundary. The geometrical remnants of the separatrix in the perturbed system are the stable (W^s) and unstable manifolds (W^u). Regions near a hyperbolic point of phase space generate chaotic behavior because the flow is ripped apart near these geometric structures, and the way the flow comes back together can be extremely complicated, as originally discovered by Poincaré [32]. According to the Smale-Birkhoff Homoclinic Theorem [33], if stable and unstable manifolds in the perturbed system intersect once transversally, they must intersect an infinite number of times, creating a "homoclinic tangle." This produces a region of "stochasticity" where the trajectory is chaotic, exhibiting sensitive dependence on initial conditions.

The hyperbolic point organizing the chaotic regions of SAM near the integrable mass ratio ($\mu = 3$) is easy to spot in the SOS. As shown in Figure 6 for $\mu = 2.95$, both the elliptic fixed point, and the hyperbolic fixed point, correspond to two separate, and coexisting, periodic "loop" orbits

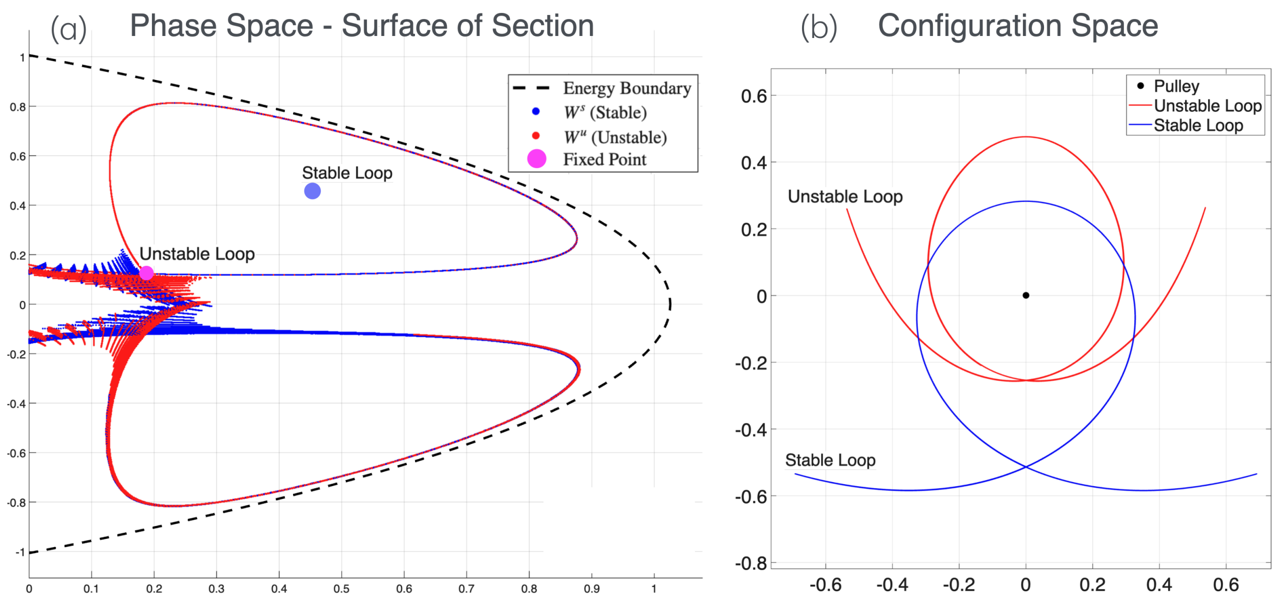

Figure 6: (a) The fixed points in phase space surface of section, and (b) their corresponding "loop" periodic orbits in configuration space. The stable loop orbit corresponds to an elliptic fixed point in phase space that organizes the main collection of KAM tori when $2.7 < \mu < 3$. Branches of the stable (W^s) and unstable (W^u) manifolds of the hyperbolic homoclinic point (purple point in (a)) delineate the main stable, and unstable, regions in phase space.

in configuration space. We call the stable orbit (blue curve in Fig. 6(b)) the "stable loop," and the hyperbolic orbit (red curve in Fig. 6(b)) the "unstable loop." By analytic continuation, we can follow these orbits back to their integrable ($\mu = 3$) locations. The stable loop at $\mu = 3$ is the central fixed point in Fig. 3(a) surrounded by elliptic tori, while the unstable loop corresponds to an orbit that starts to fall directly above the pulley ($\theta_0 = \pi$), wraps tightly around the pulley once, and then shoots upward. When it reaches the top, it falls once again and repeats. As described in [8], when $\mu = 3.0$, all the orbits of SAM in phase space are pinched between two periodic orbits – in the middle there is a (singular tori) stable loop periodic orbit which has more or less the same shape as that shown in Fig. 6b (blue curve). On the outside in phase space, surrounding all the tori, is an unstable orbit like that shown in Fig. 6b (red curve). As μ approaches 3, in configuration space the unstable loop becomes more tightly bound around the pulley and the ends of the orbit face straight up.

The unstable loop – which in the limit $\mu = 3$ collides with the pulley – is the origin of most of the unstable motion in SAM for $\mu \in [2.77, 3)$.

Problem 5: *Using a toolkit, or the codes in the supplementary material, create a surface of section plot, like those in Fig. 4, for $\mu = 2.95$. Identify the unstable loop, and the stable loop in the plot.*

5 Supplementary Material

The supplementary material package contains computer codes and simulations that provide problem solutions, and can be a useful starting point for students looking to further explore SAM's dynamics, or similar Hamiltonian systems. For instance, does the golden ratio appear in the last torus [34]?

Appendix A: Tracking Periodic Orbits

To study periodic orbits, we reduce the continuous-time dynamics to a discrete mapping by introducing a Poincaré Section, Σ. We define Σ as the plane where the swinging mass crosses the vertical axis with positive angular momentum:

$$\Sigma = \left\{ (r, \theta, p_r, p_\theta) \in \mathbb{R}^4 \mid \theta = 0,\ p_\theta > 0,\ H = E \right\} \tag{14}$$

On this section, the state is completely parameterized by the vector $\mathbf{X} = [r, p_r]^T$. The angular momentum p_θ is uniquely determined by solving $H = E$ for p_θ:

$$p_\theta = \sqrt{2r^2 \left(E - \frac{p_r^2}{2(\mu+1)} - gr(\mu - 1) \right)} \tag{15}$$

A periodic orbit of the continuous system corresponds to a fixed point of the Poincaré return map $P : \Sigma \to \Sigma$. The map $P(\mathbf{X})$ integrates Hamilton's equations from an initial state $\mathbf{X}$ on Σ until the trajectory next intersects Σ.

Finding a periodic orbit reduces to solving the non-linear root-finding problem:

$$\mathbf{F}(\mathbf{X}) = P(\mathbf{X}) - \mathbf{X} = \mathbf{0} \tag{16}$$

Our computational program uses a shooting method paired with a standard Newton-Raphson or trust-region solver. Given an initial guess $\mathbf{X}^{(0)}$, the solver iteratively refines the guess until the discrepancy $||P(\mathbf{X}) - \mathbf{X}||$ falls below a strict tolerance (e.g., 10^{-10}).

To track how the periodic orbit evolves as the system parameter μ is continuously varied from $\mu = 3.0$ down to $\mu = 2.77$, we employ zeroth-order numerical continuation.

Let $\mathbf{X}^*(\mu)$ denote the exact fixed point of the return map for a specific μ. If we change μ by a small step $\Delta\mu$, the new fixed point $\mathbf{X}^*(\mu + \Delta\mu)$ will be located close to $\mathbf{X}^*(\mu)$ assuming the orbit does not undergo a catastrophic bifurcation. The continuation algorithm proceeds as follows:

1. Start at $\mu_0 = 3.0$ with a known fixed point $\mathbf{X}^*(\mu_0)$.
2. Decrement the parameter: $\mu_{i+1} = \mu_i - \Delta\mu$.
3. Use the solution from the previous step as the initial guess for the current step: $\mathbf{X}_{\text{guess}} = \mathbf{X}^*(\mu_i)$.
4. Solve $\mathbf{F}(\mathbf{X}; \mu_{i+1}) = \mathbf{0}$ using the shooting method to find $\mathbf{X}^*(\mu_{i+1})$.
5. Repeat until the target μ is reached.

This method relies on the implicit function theorem, ensuring that a unique continuous branch of periodic orbits exists as long as the Jacobian of $\mathbf{F}$ is non-singular.

Once a periodic orbit $\mathbf{X}^*$ is found, its linear stability is determined by evaluating how small perturbations $\delta\mathbf{X}$ behave over one full period. This is governed by the Jacobian of the Poincaré map evaluated at the fixed point, also known as the Monodromy Matrix, $\mathbf{M}$:

$$\mathbf{M} = \left. \frac{\partial P(\mathbf{X})}{\partial \mathbf{X}} \right|_{\mathbf{X}^*} = \begin{bmatrix} \frac{\partial r'}{\partial r} & \frac{\partial r'}{\partial p_r} \\ \frac{\partial p_r'}{\partial r} & \frac{\partial p_r'}{\partial p_r} \end{bmatrix} \tag{17}$$

Because we lack a closed-form expression for $P(\mathbf{X})$, we estimate $\mathbf{M}$ using central finite differences. For a small perturbation $\epsilon \approx 10^{-6}$:

$$\mathbf{M}_{:,1} \approx \frac{P(\mathbf{X}^* + [\epsilon, 0]^T) - P(\mathbf{X}^* - [\epsilon, 0]^T)}{2\epsilon} \tag{18}$$

$$\mathbf{M}_{:,2} \approx \frac{P(\mathbf{X}^* + [0, \epsilon]^T) - P(\mathbf{X}^* - [0, \epsilon]^T)}{2\epsilon} \tag{19}$$

Liouville's theorem dictates that Hamiltonian phase volume is conserved, making the Poincaré map area-preserving. Consequently, the determinant of the Monodromy matrix must be identically one ($\det(\mathbf{M}) = 1$).

The eigenvalues λ_1, λ_2 of $\mathbf{M}$ are found via the characteristic polynomial:

$$\lambda^2 - \mathrm{Tr}(\mathbf{M})\lambda + \det(\mathbf{M}) = 0 \implies \lambda^2 - \mathrm{Tr}(\mathbf{M})\lambda + 1 = 0 \tag{20}$$

The solutions are completely determined by the Trace of the Monodromy matrix, $\mathrm{Tr}(\mathbf{M}) = m_{11} + m_{22}$:

$$\lambda_{1,2} = \frac{\mathrm{Tr}(\mathbf{M}) \pm \sqrt{\mathrm{Tr}(\mathbf{M})^2 - 4}}{2} \tag{21}$$

This leads to a straightforward classification of the orbit's stability:

- Elliptic (Stable): If $|\mathrm{Tr}(\mathbf{M})| < 2$, the discriminant is negative. The eigenvalues are complex conjugates residing exactly on the unit circle in the complex plane ($|\lambda_{1,2}| = 1, \lambda = e^{\pm i\phi}$). Small perturbations oscillate quasi-periodically around the fixed point.

- Hyperbolic (Unstable): If $|\mathrm{Tr}(\mathbf{M})| > 2$, the discriminant is positive. The eigenvalues are strictly real, with one eigenvalue strictly greater than 1 ($\lambda_1 > 1$) and the other less than 1 ($\lambda_2 = 1/\lambda_1 < 1$). The orbit possesses distinct stable and unstable manifolds, leading to exponential divergence of trajectories.

- Parabolic (Marginal): If $|\mathrm{Tr}(\mathbf{M})| = 2$, the eigenvalues are degenerate ($\lambda_1 = \lambda_2 = \pm 1$). This typically signals a bifurcation point where the orbit changes stability type or spawns new periodic orbits as μ is varied.

Appendix B: The Smaller Alignment Index (SALI) method

To compute the SALI, we must track the evolution of infinitesimal perturbations to the trajectory. Let $\mathbf{w}(t) = [\delta r, \delta\theta, \delta p_r, \delta p_\theta]^T$ be a deviation vector in the tangent space of the trajectory $\mathbf{X}(t)$.

The evolution of $\mathbf{w}(t)$ is governed by the Variational Equations, obtained by linearizing the vector field $\mathbf{f}(\mathbf{X})$ around the reference trajectory:

$$\dot{\mathbf{w}} = \mathbf{A}(\mathbf{X})\mathbf{w} \tag{22}$$

where $\mathbf{A}(\mathbf{X})$ is the Jacobian matrix evaluated continuously along the orbit.

The SALI computation requires the simultaneous integration of the main orbit and two independent deviation vectors.

Step 1: Initialization Choose an initial state $\mathbf{X}(0)$ on the desired energy surface. Choose two orthogonal, normalized initial deviation vectors, for example:

$$\mathbf{w}_1(0) = [1, 0, 0, 0]^T, \quad \mathbf{w}_2(0) = [0, 1, 0, 0]^T \tag{23}$$

Construct the extended 12-dimensional state vector $\mathbf{Y} = [\mathbf{X}, \mathbf{w}_1, \mathbf{w}_2]^T$.

Step 2: Integration and Normalization Integrate the extended system $(\dot{\mathbf{X}}, \dot{\mathbf{w}}_1, \dot{\mathbf{w}}_2)$ forward in time using a high-precision ODE solver.

Because chaotic dynamics will cause the magnitudes of $\mathbf{w}_1$ and $\mathbf{w}_2$ to grow exponentially, they will quickly overflow machine precision. To prevent this, the integration is performed in small time steps Δt. At the end of each step, the vectors are normalized:

$$\hat{\mathbf{w}}_1 = \frac{\mathbf{w}_1}{||\mathbf{w}_1||}, \quad \hat{\mathbf{w}}_2 = \frac{\mathbf{w}_2}{||\mathbf{w}_2||} \tag{24}$$

The normalized vectors are then used as the initial conditions for the next integration step.

Step 3: Calculating the Index At each time step t, the Smaller Alignment Index is defined as the minimum of the norms of the sum and difference of the two normalized deviation vectors:

$$SALI(t) = \min\left(||\hat{\mathbf{w}}_1(t) + \hat{\mathbf{w}}_2(t)||,\ \ ||\hat{\mathbf{w}}_1(t) - \hat{\mathbf{w}}_2(t)||\right) \tag{25}$$

The behavior of $SALI(t)$ sharply distinguishes the underlying dynamics:

- Chaotic Orbits: In a chaotic region, any arbitrary initial deviation vector will stretch and rapidly align along the most unstable manifold (the direction of the Maximal Lyapunov Exponent). As both $\mathbf{w}_1$ and $\mathbf{w}_2$ align with this same dominant direction, they become either parallel ($\hat{\mathbf{w}}_1 \approx \hat{\mathbf{w}}_2$) or anti-parallel ($\hat{\mathbf{w}}_1 \approx -\hat{\mathbf{w}}_2$). Consequently, either their difference or their sum approaches zero. Thus, for chaotic orbits, $SALI(t)$ drops exponentially to the limit of machine precision ($\sim 10^{-16}$).

- Regular (Quasiperiodic) Orbits: In a regular region, there is no exponential divergence. The deviation vectors oscillate and generally remain linearly independent, exploring the tangent space of the invariant torus. Therefore, $SALI(t)$ fluctuates around a positive non-zero constant (typically $\mathcal{O}(1)$).

By plotting $\log(SALI)$ versus time, one can visually identify the nature of the orbit often much faster than waiting for the convergence of a Lyapunov exponent calculation.

References

[1] Nivaldo A. Lemos. *Analytical mechanics*. Cambridge University Press, 2018.

[2] Olivier Pujol, José-Philippe Pérez, Jean-Pierre Ramis, Carles Simó, Sergi Simon, and Jacques-Arthur Weil. Swinging Atwood machine: experimental and numerical results, and a theoretical study. *Physica D: Nonlinear Phenomena*, 239(12):1067–1081, 2010.

[3] Nicholas Tufillaro. Smiles and teardrops. Reed College Undergraduate Thesis: https://aquahue.net/aquahue/papers/sam_00.pdf, 1982.

[4] Regilene Oliveira and Claudia Valls. Polynomial integrability of hamiltonian systems with homogeneous potentials of degree-k. *Physics Letters A*, 380(46):3876–3880, 2016.

[5] J. Casasayas, A. Nunes, and N. Tufillaro. Swinging Atwood's machine: integrability and dynamics. *Journal de Physique*, 51(16):1693–1702, 1990.

[6] Regina Martınez and Carles Simó. Non-integrability of the degenerate cases of the swinging Atwood's machine using higher order variational equations. *Discrete Contin. Dyn. Syst*, 29(1):1–24, 2011.

[7] Rafael De la Llave et al. A tutorial on KAM theory. In *Proceedings of Symposia in Pure Mathematics*, volume 69, pages 175–296. Providence, RI; American Mathematical Society; 1998, 2001.

[8] Ana Nunes, Josefina Casasayas, and Nicholas Tufillaro. Periodic orbits of the integrable swinging Atwood's machine. *American Journal of Physics*, 63(2):121–126, 02 1995.

[9] M. A. M. De Aguiar, Coraci Pereira Malta, M. Baranger, and K. T. R. Davies. Bifurcations of periodic trajectories in non-integrable Hamiltonian systems with two degrees of freedom: Numerical and analytical results. *Annals of Physics*, 180(2):167–205, 1987.

[10] M. A. M. De Aguiar and Michel Baranger. Invariant tori for two-dimensional non-integrable Hamiltonians. *Annals of Physics*, 186(2):355–380, 1988.

[11] K. Efstathiou and N. Voglis. A method for accurate computation of the rotation and the twist numbers of invariant circles. *Physica D: Nonlinear Phenomena*, 158(1-4):151–163, 2001.

[12] Robert L. Devaney. Homoclinic orbits in Hamiltonian systems. *J. Differential Equations*, 21(2):431–438, 1976.

[13] Todd Timberlake. A computational approach to teaching conservative chaos. *American journal of physics*, 72(8):1002–1007, 2004.

[14] Carles Simó. Measuring the total amount of chaos in some hamiltonian systems. *Discrete and Continuous Dynamical Systems A*, 34:5135–5164, 2014.

[15] H. R. Dullin and A. Wittek. Complete Poincaré sections and tangent sets. *Journal of Physics A: Mathematical and General*, 28(24):7157–7180, 1995.

[16] Ch. Skokos, Ch. Antonopoulos, T.C. Bountis, and M.N. Vrahatis. Detecting order and chaos in Hamiltonian systems by the sali method. *Journal of Physics A: Mathematical and General*, 37(24):6269–6284, 2004.

[17] Nicholas B. Tufillaro, Tyler Abbott, and Jeremiah Reilly. *An experimental approach to nonlinear dynamics and chaos*. Addison-Wesley Redwood City, CA, 1992.

[18] Pierre Coullet, Jean-Marc Gilli, Marc Monticelli, and Nicolas Vandenberghe. A damped pendulum forced with a constant torque. *American journal of physics*, 73(12):1122–1128, 2005.

[19] HJ Korsch, EM Graefe, and Hans-Jörg Jodl. The kicked rotor: Computer-based studies of chaotic dynamics. *American Journal of Physics*, 76(4):498–503, 2008.

[20] Steven H. Strogatz. *Nonlinear dynamics and chaos: with applications to physics, biology, chemistry, and engineering*. Chapman and Hall/CRC, 2024.

[21] N. Tufillaro and G. A. Ross. Ode - a program for the numerical solution of ordinary differential equations. Technical Report 83-52321-39, Bell Laboratories, Murray Hill, NJ, April 1983.

[22] Robert S. Maier and Nicholas B. Tufillaro. *The GNU Plotting Utilities*, 2009.

[23] George Datseris. Dynamicalsystems. jl: A julia software library for chaos and nonlinear dynamics. *Journal of Open Source Software*, 3(23):598, 2018.

[24] Matheus Rolim Sales, Leonardo Costa de Souza, Daniel Borin, Michele Mugnaine, José Danilo Szezech, Ricardo Luiz Viana, Iberê Luiz Caldas, Edson Denis Leonel, and Chris G Antonopoulos. pynamicalsys: A python toolkit for the analysis of dynamical systems. *Chaos, Solitons & Fractals*, 201:117269, 2025.

[25] Javier Roa. *Regularization in Orbital Mechanics: Theory and Practice*, volume 42. Walter de Gruyter GmbH & Co KG, 2017.

[26] Ernst Hairer, Gerhard Wanner, and Syvert P Nørsett. *Solving ordinary differential equations I: Nonstiff problems*. Springer, 1993.

[27] A. Ouazzani-TH. and M. Ouazzani-Jamil. Bifurcations of Liouville tori of an integrable case of swinging Atwood's machine. *Il Nuovo Cimento B (1971-1996)*, 110(9):1111–1121, 1995.

[28] Milovan Šuvakov and V Dmitrašinović. A guide to hunting periodic three-body orbits. *American Journal of Physics*, 82(6):609–619, 2014.

[29] G.M. Zaslavskiĭ and N.N. Filonenko. Stochastic instability of trapped particles and conditions of applicability of the quasi-linear approximation. *Soviet Journal of Experimental and Theoretical Physics*, 27:851, 1968.

[30] Regina Martínez and Carles Simó. Return maps, dynamical consequences and applications. *Qualitative theory of dynamical systems*, 14(2):353–379, 2015.

[31] Robert DeSerio. Chaotic pendulum: The complete attractor. *American Journal of Physics*, 71(3):250–257, 2003.

[32] Henri Poincaré. *The three-body problem and the equations of dynamics: Poincaré's foundational work on dynamical systems theory*. Springer, 2017.

[33] Clark Robinson. *Dynamical systems: stability, symbolic dynamics, and chaos*. CRC press, 1998.

[34] Erik M. Bollt and James D. Meiss. Controlling chaotic transport through recurrence. *Physica D: Nonlinear Phenomena*, 81(3):280–294, 1995. This paper is dedicated to the memory of Dr. Erik Bollt (1967-2025).